Fluid-induced aseismic slip may explain the non-self-similar source scaling of the induced earthquake sequence near the Dallas-Fort Worth Airport, Texas

SeongJu Jeong[1,2], Xinyu Tan[1,2], and Semechah K. Y. Lui[1,2]

[1]Department of Earth Sciences, University of Toronto, Toronto, ON, CA

[2]Department of Chemical and Physical Sciences, University of Toronto Mississauga, Mississauga, ON, CA

Corresponding author: SeongJu Jeong (seongju.jeong@utoronto.ca)

Key Points:

- Pore-pressure change induces aseismic slip with lower stress drops, either advancing or delaying seismic ruptures.
- Pore-pressure perturbation exhibits a positive correlation with aseismic-stress drops but a reversed trend with seismic-stress drops.
- Simulations show a wide spectrum of induced-slip behavior, exhibiting a similar source scaling to observations.

Abstract

Numerous studies have reported the occurrence of aseismic slip or slow slip events along faults induced by fluid injection. However, the underlying physical mechanism and its impact on induced seismicity remain unclear. In this study, we develop a numerical model that incorporates fluid injection on a fault governed by rate-and-state friction to simulate the coupled processes of pore-pressure diffusion, aseismic slip, and dynamic rupture. We establish a field-scale model to emulate the source characteristics of induced seismicity near the Dallas-Fort Worth Airport (DFWA), Texas, where events with lower-stress drops have been observed. Our numerical calculations reveal that the diffusion of fluid pressure modifies fault criticality and induces aseismic slip with lower stress drop values (<1 MPa), which further influence the timing and source properties of subsequent seismic ruptures. We observe that the level of pore-pressure perturbation exhibits a positive correlation with aseismic-stress drops but a reversed trend with seismic-stress drops. Simulations encompassing diverse injection operations and fault frictional parameters generate a wide spectrum of slip modes, with the scaling relationship of moment (M_0) with ruptured radius (r_0) following an unusual trend, $M_0 \propto r_0^{4.4}$, similar to $M_0 \propto r_0^{4.7}$ observed in the DFWA sequence. Based on the consistent scaling, we hypothesize that the lower-stress-drop events in the DFWA may imply less dynamic ruptures in the transition from aseismic to seismic slip, located in the middle of the broad slip spectrum, as illustrated in our simulations.

Plain Language Summary

Injection-induced earthquakes have presented significant obstacles to developing energy resources related to fluid injection, such as enhanced geothermal systems and shale gas development. Despite their prevalence, the causes and impact of these earthquakes are not fully understood. Aseismic slip, characterized by slower velocities and longer durations than typical earthquakes, has been observed in induced earthquake studies. In this study, we use a numerical model to investigate how fluid pressures influence the slip properties of induced seismicity near the Dallas-Fort Worth airport (DFWA), Texas. Our model shows that elevated fluid pressure induces aseismic slip and advances or delays fast slip (i.e., earthquakes). The pore-pressure perturbation alters the source characteristics of both aseismic-slip events and seismic ruptures, enhancing aseismic-stress release while diminishing seismic-stress release. Simulations involving various fault frictional properties reveal a wide spectrum of slip modes, ranging from slow to rapid slip, which are different from the stress-release processes that drive globally observed natural earthquakes, but exhibit similarities to observations in the DFWA. Consequently, we infer that the DFWA events may exhibit reduced dynamic characteristics akin to slow slip events positioned in the middle of the broad spectrum generated in our modeling.

1. Introduction

Fluid injection into the subsurface is an important industrial practice used for developing geo-energy resources such as enhanced geothermal systems, CO_2 sequestration, and shale gas extraction worldwide (National Research Council, 2013). However, these injections often induce seismicity, leading to the suspension of several projects (e.g., Pohang in Korea, Basel in Switzerland, and the 2011 Preese Hall in UK) (Häring et al., 2008; Foulger et al., 2018; Lee et al., 2019). Thus, seismic hazard assessment and understanding the slip properties of induced earthquakes are essential for sustainable energy development.

Injection-induced earthquakes are commonly accepted to be induced by at least two main mechanisms: (1) elevated pore pressure that diffuses through rock pores and directly reduces effective normal stress (frictional resistance to slip) on pre-existing faults, and (2) poroelastic coupling, which is an elastic deformation of a porous medium that indirectly alters fault-loading conditions without hydraulic connection (Ellsworth, 2013). However, the triggering mechanisms associated with pore-pressure changes alone remain controversial in explaining why geodetic observations have often detected aseismic slip (e.g., Eyre et al., 2022; Jiang et al., 2022; Pepin et al., 2022; Staniewicz et al., 2020), which require further interpretation of fault dynamics.

In addition to geodetic observations, a field-scale experiment in southeastern France has recorded aseismic slip using specially designed strainmeters, indicating that pore-pressure increases initially triggered aseismic slip on pre-existing faults (Cappa et al., 2019; Guglielmi et al., 2015). Numerical modeling conducted for this experiment has complemented the observed aseismic slip (Bhattacharya and Viesca, 2019; Larochelle et al., 2021). The source characteristics of the microseismicity ($-3.9 < M_{\mathrm{W}} < -3.1$) in this experiment show low-stress drops (~0.01 MPa on average), which may suggest the occurrence of slow earthquakes influenced by the aseismic response and fluid pressure increases (Huang et al., 2019). Several seismological observations have also reported events with lower-stress drops for induced earthquakes (Chen & Abercrombie, 2020; Goertz-Allman et al., 2011; Jeong et al., 2022; Shen et al., 2023; Yu et al., 2021). These lower-stress-drop events are mainly found at the beginning of the sequence and in proximity to injection wells, often giving rise to an apparent non-self-similar scaling of induced earthquakes. The apparent scaling observations may result from changes in fault friction behaviors influenced by pore pressure unless rock material properties (i.e., seismic velocities) vary in space. For instance, Jeong et al. (2022) observed a magnitude dependence and distance trend in stress drops of the earthquake sequence at Dallas-Fort Worth Airport (DFWA), Texas (Figure 1), which predominantly occurred in the basement, assumed to possess consistent rock properties. The low-stress drops may indicate a dynamic weakening of the fault, which may be influenced by an increase in pore pressure and a reduction in effective normal stress (Goertz-Allman et al., 2011). The decrease in effective normal stress leads to a lower degree of interface locking on the fault and limits the magnitude of stress drops (Moreno et al., 2010). This may imply different slip behaviors on the pre-existing fault in response to fluid injection (e.g., De Barros et al., 2023).

In a tectonic environment, aseismic slip often occurs in combination with pore-pressure diffusion, contributing to the moment budget and release of the strain accumulated on the fault (Durand et al., 2022; Ruhl et al., 2016). Studies in subduction zones suggest that aseismic creep can initiate or trigger large seismic ruptures and may be considered a precursor event for forecasting large earthquakes (Harris, 2017; Obara & Kato, 2016). Thus, aseismic slip plays a crucial role in altering the timing of earthquake occurrence, subsequent seismic cycles, and earthquake hazard assessment (Bürgmann, 2018; Lui et al., 2021). These findings highlight the importance of coupled modeling of dynamic ruptures and fluid pressure evolution to better understand the role of aseismic slip and the complex processes involved in injection-induced seismicity.

This study investigates the influence of pore pressure diffusion resulting from fluid injection on fault slip activation, dynamic behavior, and source scaling. The observations in the

DFWA are used to establish a numerical simulation and to constrain model parameters such as bottomhole pressure, reservoir properties, and fault framework. To account for both aseismic and seismic fault-slip behavior, we employ the spectral boundary integral method with a rate-and-state friction and pore-pressure diffusion model under stable tectonic loading. We simulate the model both with and without fluid injections and subsequently extend the simulations by varying injection operation scenarios and fault frictional parameters to gain insights into the characteristics of triggered slip, their source properties, scaling relationships, and their impact on subsequent seismicity.

2. Models and Methods

To simulate the dynamic behaviors and source parameters of DFWA-induced seismicity, we use findings from previous studies to construct a model framework and constrain model parameters, including fault length, asperity size, shear wave velocity, shear modulus, and hydraulic parameters. Subsequently, the rate-and-state friction and pore pressure diffusion are incorporated into the DFWA fault model for simulations using spectral boundary integral equations.

2.1. Induced Seismicity in the DFWA

DFWA was previously considered an area of low-tectonic deformation over the past 300 Ma (Magnani et al., 2017). However, induced seismicity began to occur with the development of unconventional oil and gas production since 2008 (Frohlich et al., 2011; Ogwari et al., 2018). The initial sequence starting in October 2008 involved 10 events ($2.6 < M < 3.0$) observed by the regional seismic network. Subsequently, a local seismic network installed by Southern Methodist University recorded 11 swarm-like earthquakes with high sample-rate data (200 samples/second) between November 20 and December 2, 2008 (DeShon et al., 2019). The majority of the earthquakes (9 out of 11 events) occurred within a span of 3 hours on November 20, 2008, while the remaining two were detected on November 28 and December 1 of the same year. Although the fault length in the DFWA exceeds 50 km (Hennings et al., 2019; Horne et al., 2020), these events occurred in the vicinity of the nearest injection well (API 42-439-32673) and traced a ~1 km linear feature that was parallel to a pre-existing fault (Figure 1a). Jeong et al. (2022) estimated lower-stress-drop values for the 11 DFWA earthquakes and abnormal source scaling, with stress drops increasing with moment magnitude and radial distance from the injection point within the first 1.5 km (Figures 1b, c). The DFWA fault is optimally oriented in the regional stress field, meaning that small stress perturbations can potentially nucleate earthquakes along the fault (Hennings et al., 2019). Fluid injection began at the nearest well in September 2008, prior to the earthquakes, and was subsequently shut down in August 2009, resulting in about a year of injection. Ogwari et al. (2018) demonstrated that seismicity continued to migrate mainly towards the northeast, parallel to the pore-pressure-diffusion front. The earthquake depths are ~4.5 km below sea level (Frohlich et al., 2011) within a crystalline basement composed mainly of granite and diorite (Smye et al., 2019). The injection depth interval of interest is shallower, ranging from 3.1 to 4.2 km.

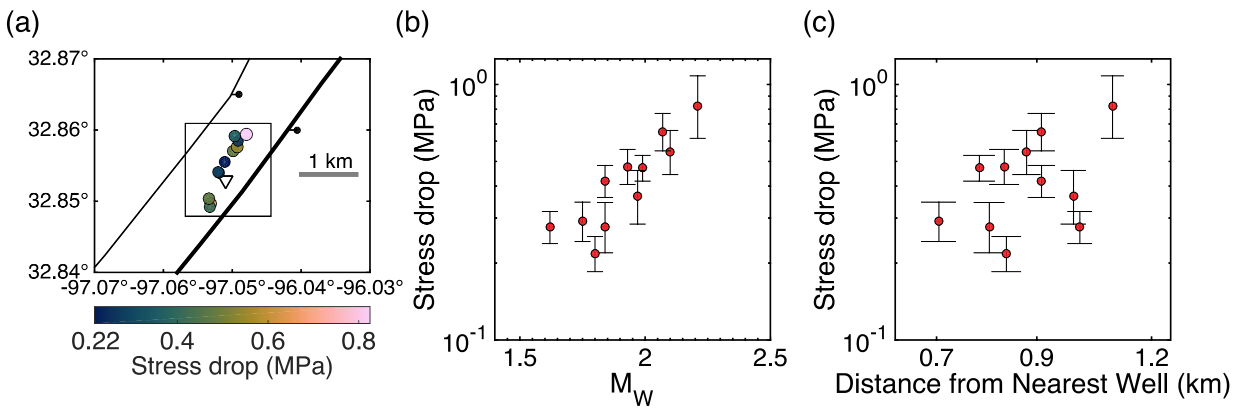

Figure 1. Seismic characteristics of the Dallas-Fort Worth Airport (DFWA), including (a) a map of the seismicity, stress-drop estimates increasing with (b) moment magnitude M_W, and (c) radial distances from the nearest injection well. In (a), black lines depict faults and black dots represent the downthrown hanging-wall block from Horne et al. (2020). The seismogenic fault is highlighted as the bold line, and the inverted triangle indicates the location of the injection well. The rectangle represents a resized fault shown in Figure 2. In (b, c), the error bars represent the 95% confidence limits. The figures have been modified from Jeong et al. (2022).

2.2. Simulating Earthquake Sequences using Rate-and-State Friction

We simulate dynamic earthquake sequences using the spectral boundary integral equation method, which resolves both aseismic and seismic slip on faults (Lapusta et al., 2000). Our model implements the long-term evolution of slip and stress along the fault, taking into account inertial effects during rapid seismic events. Thus, the model results in a fully dynamic process, in which the stress is redefined from the final stress of the previous event after an earthquake rupture. Friction on the fault is controlled by the laboratory-derived rate-and-state friction law, which represents the evolution of friction depending on slip velocity (V) and frictional state variable (θ) (Dieterich, 1979; Marone, 1998; Ruina, 1983). The fault slip is governed by the fault strength τ_f given by

$$\tau_f = (\sigma_n - p)\left[f_0 + a\ln\left(\frac{V}{V_0}\right) + b\ln\left(\frac{V_0\theta}{d_c}\right)\right] \quad (1)$$

where σ_n represents the normal stress, p is the pore pressure, f_0 is a reference friction coefficient, V_0 is the reference velocity, and d_c is the critical slip distance. Parameters a and b are the frictional stability factors for the direct effect of changes in V and the evolutionary effect of θ, respectively. To estimate the evolution of θ, two choices are available: the aging law and the slip law. The aging law describes the response of asperities to long contact time (Dieterich, 1979) and is widely used in various numerical studies (e.g., Lapusta et al., 2000, Lin, & Lapusta, 2018, Lui et al., 2021). The slip law simulates nucleation processes better for interactions between aseismic and seismic events (Ampuero and Rubin, 2008). We compare models with two evolution laws in Supporting information (Text S1 and Figures S1-S3). The results from both laws are qualitatively consistent with each other. As a result, we opt for the aging law, which appears more favorable for investigating aseismic slip. The aging law is given as

$$\frac{\partial \theta}{\partial t} = 1 - \frac{V\theta}{d_c}\,. \tag{2}$$

At steady state, $\theta = d_c/V$, the fault strength τ_s is rewritten as

$$\tau_s = (\sigma_n - p)\left[f_0 + (a-b)\ln\left(\frac{V}{V_0}\right)\right]. \tag{3}$$

Regions with $(a-b) > 0$ are velocity-strengthening (VS), which are mostly creeping steadily. On the other hand, regions with $(a-b) < 0$ are velocity-weakening (VW), which promotes earthquake nucleation and rupture propagation. The rate-and-state friction properties (a, b, and d_c) are assumed to be constant and independent of pore-pressure perturbations. Due to limited frictional information for the DFWA fault, we adopt the $(a-b)$ values for granite gouge under hydrothermal conditions at a depth of 5 km: $(a-b) = +0.004$ and -0.004 for the VS and VW regions, respectively (Blanpied et al., 1991, 1995). The initial shear stresses in the VS and VW regions, τ_0^{VS} and τ_0^{VW}, are determined from equation 3 with V equals tectonic loading (V_{pl}).

Dynamic rupture nucleates when the slipping region on the VW patch exceeds the nucleation size (h^*) suggested by Rubin & Ampuero (2005) as

$$h^* = \frac{2}{\pi}\frac{\mu_s^* b d_c}{(b-a)^2(\sigma-p)} \tag{4}$$

where $\mu_s^* = \mu_s$ for mode III ruptures and $\mu_s^* = \mu_s/(1-\nu)$ for mode II ruptures, where μ_s is the shear modulus and ν is the Poisson's ratio.

We set up a 1D planar fault with a length of 1,000 m (L_x) based on observed seismicity (Figure 1a). This fault is embedded in a homogeneous 2D medium, and thus we resolve a 2D antiplane shear problem (Figure 2). We assume the presence of a hydraulic pathway between the injection wellbore and the fault surface, and thus fluid is directly injected onto the fault (Figure 2). The VW patch is located in the center of the fault and surrounded by VS regions under tectonic loading. The expected tectonic loading at DFWA is as slow as 1-2 mm/year (Kreemer et al., 2018, Wang et al., 2022). However, in order to model pore-pressure effects on multiple seismic cycles, for computational efficiency, we use a faster loading rate of 23 mm/year. In Supporting information (Text S2 and Figures S4-S6), we compare the results obtained with slower and higher loading rates and find that changes in the loading rate alter the recurrence interval but do not pose substantial changes to the general slip pattern or the aseismic and seismic source properties. The diameter of the VW patch (d) is set to 200 m, determined from the average rupture radius of 100 m estimated by Jeong et al. (2022). The shear wave velocity (C_s) and shear modulus at the fault depth are based on previous studies of seismicity in north Texas (Quinones et al., 2018, 2019). We simulate the earthquake cycle for 15 years with an adaptive time step, which results in a much shorter time step during dynamic ruptures relative to interseismic periods (Lapusta et al., 2000; Lapusta & Liu, 2009). The threshold of seismic rate is set to 0.01 m/s, following Chen & Lapusta (2009), while the aseismic slip is empirically defined by a threshold of 1.46×10^{-9} m/s, twice the value of V_{pl} (Figure 3). Detailed fault parameters are documented in Table 1.

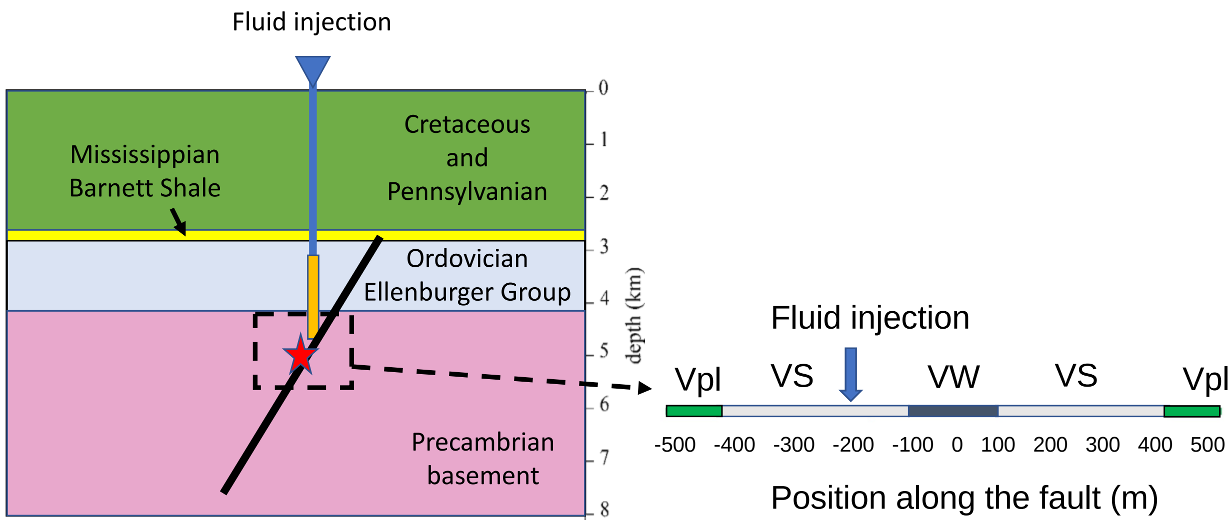

Figure 2. Schematic illustration of the fault framework. The actual fault (black line) extends in depth between 3 and 7 km across multiple layers. However, we reduce the fault size (dashed rectangle) based on the seismicity displayed in Figure 1a, where the center of seismicity is denoted by the red star in this figure. The modified fault is situated within the basement. The right-hand side of the figure illustrates the resized fault layout, consisting of a 1 km long fault with a 200 m diameter velocity-weakening (VW) asperity at the center (dark gray) and two 300 m velocity-strengthening (VS) regions on both sides (light gray). The VW area is determined from the average rupture radius of 100 m estimated by Jeong et al. (2022). The actual injection point is above the fault, but we assume the existence of a hydraulic conduit (vertical orange line) between the actual injection point and a location -200 m from the center of the fault, which emulates direct injection onto the fault. The edges of the fault are loaded by a tectonic slip rate (V_{pl}) of 23 mm/year (green).

2.3. Simulating Pore-Pressure Diffusion

To simulate induced seismicity, we integrate pore-pressure diffusion into the rate-and-state fault model. Since the pore pressure is time-dependent, the diffusion calculation is incorporated at identical grid points as the spectral boundary integral equations. The 1D fluid transport equation is given by

$$\frac{\partial p}{\partial t} = \frac{\partial}{\partial x}\left[D\,\frac{\partial p}{\partial x}\right] + G \tag{5}$$

where p is pore pressure, D is hydraulic diffusivity, and G represents the potential source at the injection location and time. The hydraulic diffusivity is estimated using the equation $D = \frac{k\rho g}{\eta S}$ where k is permeability, ρ is density, g is gravitational acceleration, η is viscosity, and S is specific storage. We take these parameters based on previous research conducted in Azle, Texas, which is assumed to have similar geomechanical characteristics to the DFWA area (Hornbach et al., 2015). The potential source is determined from bottomhole pressure estimated from surface pressure using an algorithm described in Gao et al. (2021). The average rate of bottomhole pressure is 17.4 Pa/s, which is directly injected into the VS region situated 200 m away from the center of the fault as a constant fluid source (see Figure 2). For simplicity, we neglect changes in porosity and permeability. Several studies have proposed that permeability changes can contribute to slow slip earthquakes and variations in fluid-induced seismicity (Khajehdehi et al., 2022, Marguin & Simpson, 2023). To investigate the effect of permeability changes, we conduct an additional simulation with a simple permeability evolution (Text S3 and Figure S7) and find that permeability changes have no significant impact on our modeling results.

We solve the pore-pressure changes using the explicit finite difference method. To ensure numerical stability, we use Von Neumann stability analysis, $\frac{D\Delta t}{\Delta x^2} < \frac{1}{2}$ where Δt and Δx are time and spatial resolutions, respectively. After the injection begins, the time resolution follows that of fluid injection (Δt) until the simulation is completed. This accounts for a leftover effect from the continued diffusion of the pore-pressure front along the fault even after injection stops. Due to the short time resolution required for dynamic ruptures, the pore-pressure perturbations are not processed during seismic ruptures. We omit the first event to avoid effects from initial conditions, and thus the fluid injection begins after the foremost seismic rupture. We also neglect poroelastic effects, which are relatively smaller than pore-pressure perturbations at the length scale of the model and for the relatively short simulation time (Zhai & Shirzaei, 2018). The detailed parameters of pore-pressure diffusion are given in Table 1.

Table 1. Model Parameters

Parameter description	Symbol	Value
Shear wave speed	C_s	3,460 m/s
Shear modulus	μ_s	32 GPa
Loading slip rate	V_{pl}	23 mm/year (7.29×10^{-10} m/s)
Reference slip velocity	V_0	10^{-6} m/s
Reference friction coefficient	f_0	0.6
Characteristic slip distance	d_c	160 μm
Initial shear stress in VS and VW regions	$\tau_0^{VS},\ \tau_0^{VW}$	31.4 MPa, 28.5 MPa
Initial normal stress	σ_n	50 MPa
Fault length	L_x	1,000 m
Patch diameters	d	200 m
Nucleation size	h^*	78 m
Rate-and-state properties in VS region	a, b	0.015, 0.011
Rate-and-state properties in VW region	a, b	0.015, 0.019
Spatial resolution	Δx	0.28 m
Fluid injection rate	G	17.4 Pa/s
Permeability	k	1.0×10^{-15} m^2
Fluid density	ρ	1,031 kgm^{-3}
Gravitational acceleration constant	g	9.81 m^2/s
Fluid viscosity	η	1.1×10^{-3} $Pa\ s$
Specific storage	S	13×10^{-6} m^{-1}
Hydraulic diffusivity	D	7.1×10^{-4} m^2/s
Time resolution for pore-pressure model	Δt	55.6 s

3. Results

3.1. Aseismic-Slip Events

We simulate the earthquake cycle and estimate the maximum slip velocity (V_{max}) over time using the rate-and-state friction fault model, considering both scenarios: (1) with and (2) without fluid injection (Figure 3). Here, the earthquake cycle without fluid injection serves as a reference, which only experiences seismic ruptures with consistent recurrence intervals of ~1.75 years (Figure 3a). When fluid is injected at year 8.47 (50% of the recurrence interval after the first earthquake), we observe that the pore-pressure perturbation leads to advanced timing of seismic activities compared to the reference scenario. The recurrence times in the fluid-injection scenario exhibit variation after injection but gradually converge toward the event timings observed in the reference scenario after the suspension of fluid injection. This suggests that fluid-driven stress perturbations gradually subside to background levels after injection stops, and the stress states surrounding the fault recover to tectonic conditions through multiple earthquakes over time.

Shortly after injection begins, we observe two slow-slip events before the seismic rupture that are characterized by relatively smaller velocities and longer durations (Figure 3b). The amplitude and duration of V_{max} are 3.6×10^{-9} m/s and 13.7 days for the first aseismic-slip event. For the second event, the amplitude is 6.6×10^{-9} m/s, with almost identical duration to the first one. After injection ceases, one more aseismic-slip event is observed just before the post-injection-seismic rupture occurs (Figure 3c), with amplitude and duration of 2.9×10^{-8} m/s and 13.1 days. In this case, the subsequent seismic rupture begins before V_{max} falls back to V_{pl}. This suggests that aseismic slip may play a significant role in triggering earthquakes. Note that the duration of seismic ruptures ranges from 0.5 to 2 seconds.

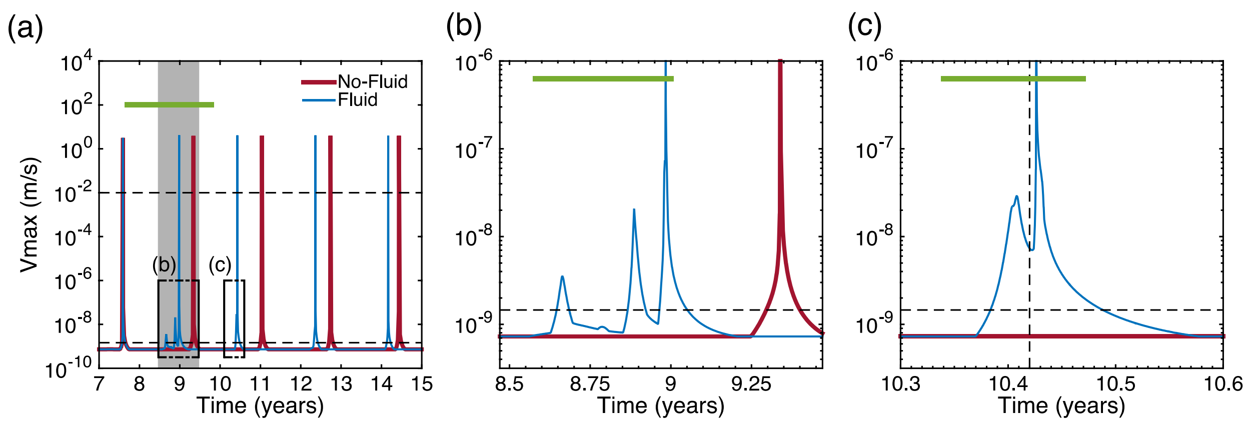

Figure 3. Maximum slip velocities (V_{max}) plotted against simulation time for a fault length of 1,000 m with a 200 m diameter VW asperity. Two scenarios are simulated: one without fluid injection (red) and one with fluid injection (blue). (a) displays V_{max} over 7 to 15 years. Note that no seismic events are triggered before year 7. The gray-shaded area highlights the time range for fluid injection, spanning from 8.47 to 9.47 years. (b) zooms in on the injection period including the first and second aseismic-slip events depicted in (a). (c) zooms in on the period including the third aseismic slip in (a), which is considered to end at year 10.42 (vertical dashed line). The

horizontal dashed lines denote the seismic (10^{-2} m/s) and aseismic (1.46×10^{-9} m/s) velocity thresholds. Green horizontal bars highlight the time windows shown in Figure 4.

To investigate these aseismic-slip events in more detail, we analyze changes in pore pressure, slip rate, and shear stress (Figure 4). In our reference simulation with only tectonic loading, earthquakes rupture the entire VW asperity, and there is little variation during the interseismic period on the fault (Figure 4a). In contrast, with fluid injection, pore-pressure perturbation triggers two aseismic-slip events, partially releasing the cumulative stress prior to seismic rupture (Figure 4b and Figure S8a in Supporting information). The first and second events nucleate at 151.2 m and 169.0 m from the injection point, respectively, both within the left side of the VW region that is closer to the injection source and affected more strongly by pore-pressure diffusion. After the suspension of injection, the pore-pressure diffusion front continues to propagate, triggering the third aseismic-slip event at 180.2 m from the injection point, followed by subsequent seismic rupture at the center of the fault (Figures 4c and S8b). This suggests that the asperity is still heavily influenced by pore-pressure perturbation even after injection stops.

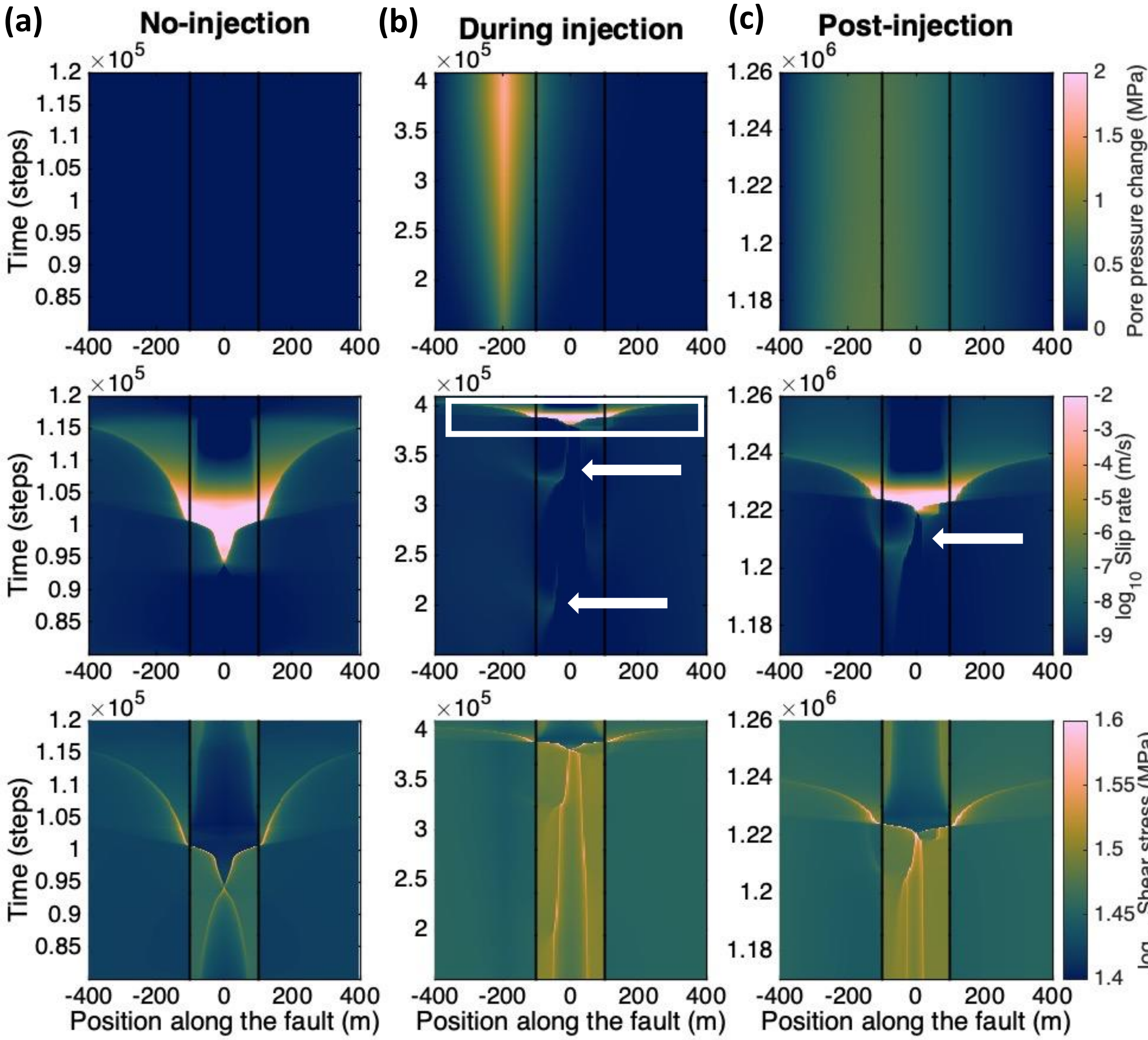

Figure 4. Pore-pressure diffusion (top), logarithmic slip rate (middle), and logarithmic shear stress (bottom) on the fault with simulation time steps for two scenarios: (a) model with no injection and (b, c) model with fluid injection at -200 m from the center of the VW asperity, as illustrated by black vertical lines. The time windows for each column are highlighted in Figure 3 (green horizontal lines). In the middle row of (b), white box represents a seismic rupture, as shown in Figures 5a-c. In (b, c), white arrows indicate the aseismic-slip events. Note that the colorbar in the middle row (i.e., slip rate) is constrained to 10^{-2} m/s, a criterion used for determining seismic rupture, in order to maintain visually distinct aseismic slip events.

Next, we define the rupture domain for both aseismic and seismic events to investigate the rupture characteristics shown in Figure 4. Figures 5a-c illustrate the distribution of cumulative slip, slip rate, and shear stress changes along the fault for the seismic rupture that occurred during the injection period, starting at year 8.98 and lasting for 0.66 seconds. The rupture domain (Σ) represents the region with a net positive slip and is defined as $\Sigma_{\mathrm{seis}} = \{x \in$

$L_x|\delta(x) > 0\}$ for seismic events (Figure 5a). Note that ruptures in our simulations extend from VW into neighboring VS regions, and hence result in a complex shear stress change profile along fault.

In the case of aseismic-slip events, non-zero slip is widely observed both within and outside the VW patch (Figures 5d, g, j). The first, second, and third aseismic events start at years 8.65, 8.87, and 10.38, respectively, and each lasts ~13 days (see Figure 3). Since we defined the aseismic-slip velocity threshold as 1.46×10^{-9} m/s, the duration of each slow slip event is defined as the period of time when the V_{max} of the fault exceeds this threshold. Similarly, for aseismic slip events, Σ is determined at locations where the slip rate exceeds 1.46×10^{-9} m/s during the events, defined as $\Sigma_{\text{aseis}} = \{x \in L_x|V(x) > 1.46 \times 10^{-9}\ m/s\}$, following the methodology by Perry et al. (2020) (Figures 5e, h, k). The rupture dimensions are 51.3 m, 162.8 m, and 158.3 m for the first, second, and third aseismic-slip events, respectively. The second and third events are generally half of the size of seismic ruptures (303.3 m). However, the first aseismic event shows a significantly smaller rupture dimension, probably due to the relatively lower extent of pore-pressure perturbation at that time (Figures 4 and S8).

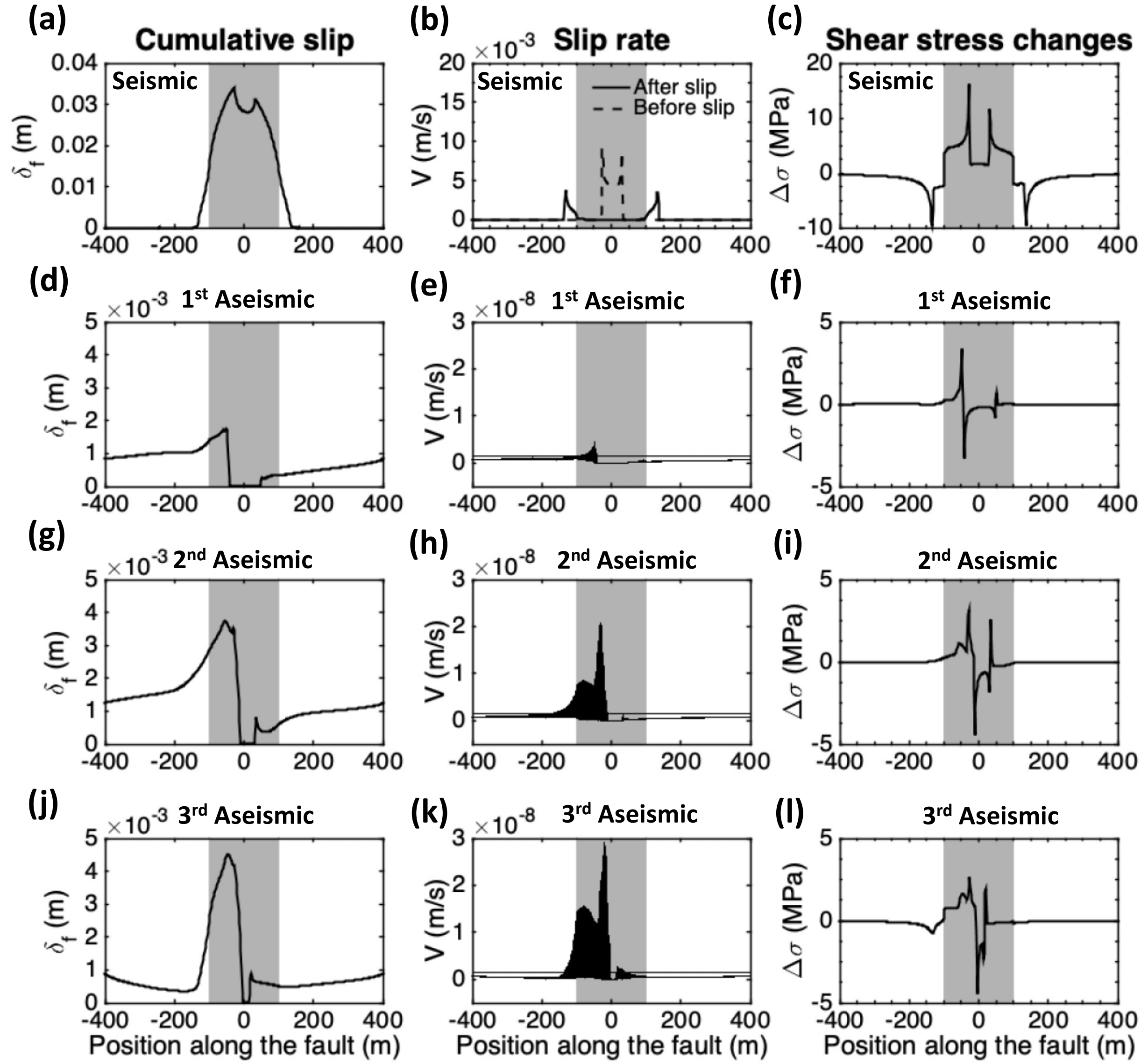

Figure 5. Distribution of cumulative slip (left), slip rate (middle), and change in shear stress (right) in three columns as a function of position along the fault for (a-c) seismic ruptures and (d-l) aseismic-slip events. The seismic rupture starts at year 8.98 and lasts for 0.66 seconds (white box in the middle row of Figure 4b). The first (d-f), second (g-i), and third aseismic events (j-l) start at years 8.65, 8.87, and 10.38, respectively, and each lasts ~13 days (white arrows in the middle row of Figures 4b,c). In the middle column, (b) displays slip rates before and after the seismic event, while (e, h, k) show the stacking of the slip rate profile along the fault at all time steps during aseismic events. Horizontal lines in (e, h, k) represent the threshold of aseismic slip (1.46×10^{-9} m/s). The VW asperity is highlighted as the gray-shaded area.

3.2. Stress-Drop Variation

We estimate source parameters for the simulated events. The average stress drop based on energy considerations, $\Delta\sigma_E$ (Noda et al., 2013), is given as

$$\Delta\sigma_E = \frac{\int_\Sigma \Delta\sigma(x)\delta_f(x)d\Sigma}{\int_\Sigma \delta_f(x)d\Sigma} \tag{6}$$

where $\Delta\sigma(x)$ is the distribution of shear stress changes and $\delta_f(x)$ is the final slip distribution, which is used as a weighting function. The weighting function has a maximum value of 1 and defines the rupture domain. This method presents a simple way of calculating stress drop for events with complex rupture domain, such as aseismic-slip events in this study (Figures 5d, g, j). The effective source radius (r_0) is determined based on the ruptured domain defined in section 3.1 as $r_0 = \sqrt{\Sigma^2/\pi}$ (Schaal & Lapusta., 2019) for a circular crack model (Eshelby, 1957). The moment is estimated as

$$M_0 = \frac{16}{7}\Delta\sigma_E r_0^3. \tag{7}$$

Here, we also calculate the average pore-pressure values using the same method employed for calculating stress drop, replacing distribution of shear stress changes with pore-pressure distribution in equation 6.

Figure 6 depicts the variation in seismic moment and average stress drop values. For a no-injection scenario, the source parameters of seismic ruptures are consistent with each other and remain independent of time. In the case of fluid injection, we observe both seismic and aseismic events with a wide range of stress drops and moments. Interestingly, among just the triggered seismic events, there is a weak positive trend in stress drop and moment, as shown in the inset in Figure 6c, which is similar to field observation. When considering the triggered aseismic transients, which have lower moments and stress drops than seismic ruptures, it becomes clear that the positive trend continues. For the three aseismic transients, we observe temporal increases in both moments and stress drops, similar to the findings of V_{max} (Figures 3b, c). The larger stress drops observed for the later aseismic-slip events suggest a change in fault criticality, which can be explained by equation 4. Since effective normal stress decreases due to enhanced pore pressure, it contributes to the growth of nucleation size and a reduction in the VW-diameter-to-h^* ratio, favoring aseismic-stress release. In fact, the estimated pore-pressure values are 0.07, 0.18, and 0.58 MPa for first, second, and third aseismic slip events, respectively, indicating a correlation between pore pressure and stress drop values (Figure 6d) and providing support for the hypothesis of nucleation growth. The initial phase of aseismic slip promotes local stress transfer and likely causes the variation in stress drop in subsequent seismic events. Consequently, the trend of seismic events with respect to pore pressure is reversed (slope = -0.1), as shown in the inset of Figure 6d, due to aseismic-stress release, resulting in reduced seismic-stress release.

Note that the stress drops of aseismic-slip events also show a positive trend with the distance from the injector. Here the distance from the injection point is estimated as the separation between the injection location and V_{max} on the ruptured area for all simulated events. In general, pore-pressure changes peak at the injection source and decrease with radial distance, while pore pressure increases with time at a given point on the fault as injection continues. Based on the positive correlation between pore-pressure values and aseismic stress drop, the increase in stress drop with the distance is likely a reflection of the temporal diffusion of pore pressure. In contrast, the negative correlation between pore-pressure values and seismic stress drops suggests the increase in stress drop with distance may be predominantly the effect of spatial decay of pore-pressure from the injection source, consistent with the observations in the DFWA sequence, where the first 9 events occurred within only ~3 hours.

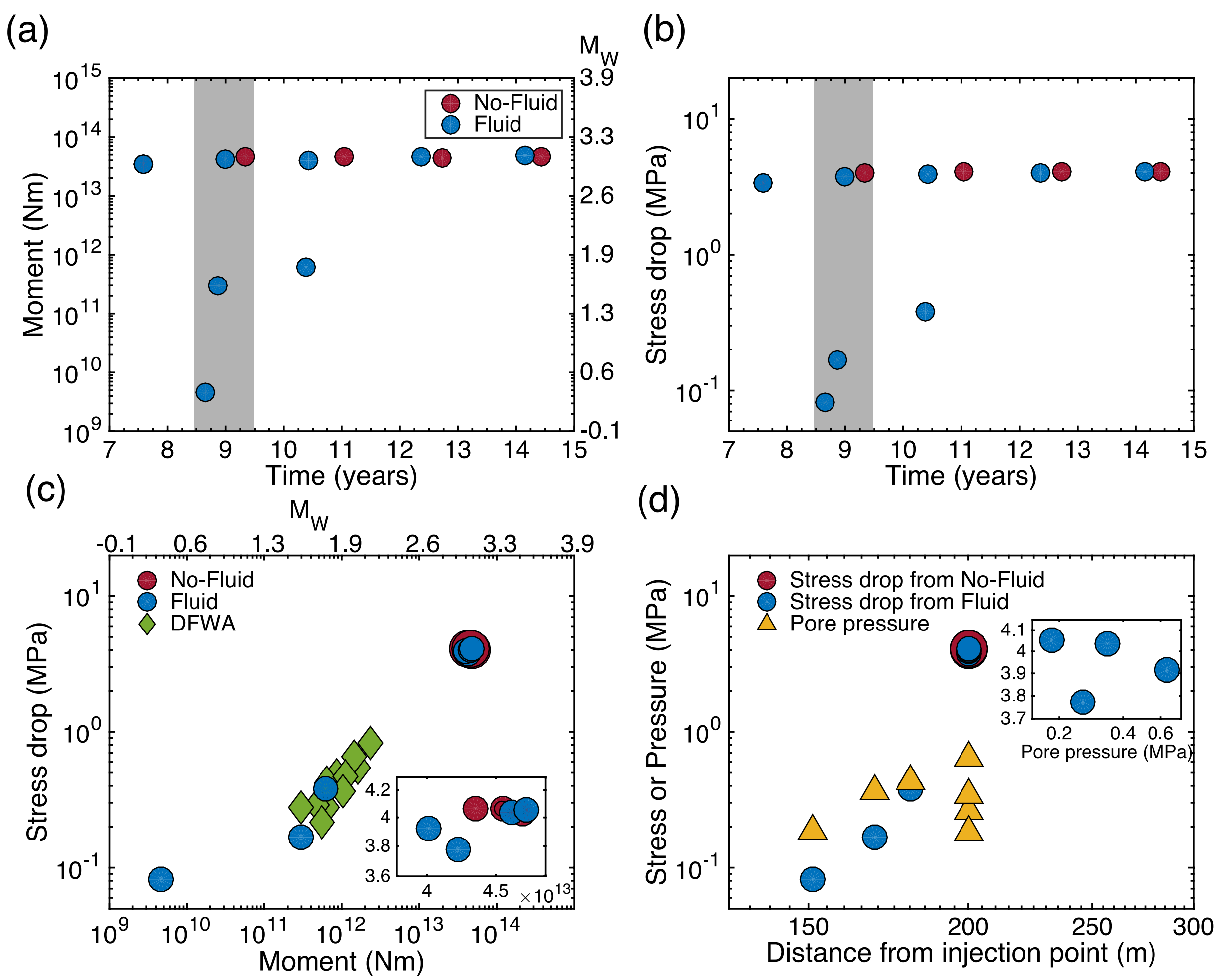

Figure 6. Analysis of source parameters from simulated events, including the temporal variation of (a) seismic moment and (b) stress drop. Stress-drop values are also plotted against (c) seismic moment and (d) distance from the injection point. The simulations include scenarios with (blue) and without (red) fluid injection. In (a,b), the gray-shaded area highlights the duration when fluid injection occurs. In (c), the green diamonds represent the observed stress drops in the DFWA sequence (Jeong et al., 2022). The inset in (c) shows a zoomed-in view of seismic ruptures, highlighting stress drop variation in the fluid-injection scenario compared to the no-injection model. In (d), average pore-pressure changes (yellow triangles) are measured during the same time periods as the stress-drop estimates. The inset in (d) displays stress drop as a function of pore-pressure changes only for seismic ruptures. Note that the first simulation event has been removed from (c) and (d) to eliminate initial model effects.

3.3. Triggered Slip Behavior and Source Parameter Scaling under Various Injection Conditions and Fault Frictional Properties

To further investigate the sensitivity of our numerical observations to various injection scenarios and fault frictional states, we perform a suite of simulations and analyze the resulting slow slip and earthquake characteristics. Here, the original model with fluid injection is used as a reference, which is based on the reported injection rates.

3.3.1 Effects of Injection Operation Parameters

First, we compare the effects of various injection locations at -100, -200, and -300 m from the fault center (Figures 7a, b). Note that the negative sign denotes the left-hand side of the VW patch (Figure 2). At the closer distance of -100 m, both aseismic slip and seismic ruptures occur earlier than the reference, while at the longer separation of -300 m, the events are delayed. The recurrence times of seismic ruptures at the -100 m injection are comparable to the reference (0.03 to 0.1 years difference), while at the -300 m injection, they are longer (0.1 to 0.3 years). However, the recurrence time among the three cases gradually converages after multiple earthquake cycles. The intensity of aseismic slip also follows the same pattern as the reference model shown in Figure 3, where the first aseismic-slip event has a lower amplitude than the second (Figure 7b). The increase in V_{max} over time for each aseismic-slip event may be related to a temporal increase in pore pressure, which correlates with stress drop (Figure 6d). This result suggests that an increase in pore pressure promotes a rapid slip rate and leads to a larger energy release for aseismic slip. For the 300 m separation, only one aseismic-slip event is found, suggesting that the separation influences not just the intensity but also the number of aseismic-slip events.

Second, we modulate the injection volume to values that are a factor of two larger than the reported injection rate (Figures 7c, d). The higher fluid pressure leads to earlier occurrences of aseismic slip and seismic rupture. During the injection period, V_{max} for two aseismic-slip events exceeds those in the reference model by a factor of 4 for the first event and 2 for the second event (Figure 7d). Following the cessation of injection, the scenario with a larger injection volume shows significant variations in the first two seismic events (at years 9.6 and 12.0 in Figure 7c), a difference in recurrence intervals by a factor of 3. We found that the fault maintains a higher V_{max} than V_{pl} during the short interseismic period (0.74 years), indicating that the pore pressure effect remains significant after injection ends. During the longer interseismic period (2.40 years), we observe two occurrences of slip-rate elevation (Figure S9). Although they are below the aseismic threshold set in this study, they likely release considerable stress on the fault and delay the next seismic event.

Third, we investigate different injection durations of 3, 6, and 12 months (Figures 7e, f). A short injection duration of 3 months leads to a delay in seismic triggering associated with a small aseismic slip, which is lower V_{max} than the aseismic criteria specified in this study. Consequently, we exclude this event from the analysis. Both aseismic and seismic events triggered by the 6-month duration do not differ significantly from the reference (12-month period) during the injection phase, but the occurrence of post-injection event is further delayed, at year 10.79, compared to the reference model at year 10.43. The advancement of post-injection events suggests that an extended injection window may lead to a greater pore-pressure perturbation after injection cessation, exerting a stronger influence on the earthquake cycle.

Lastly, fluid is injected into our model at various times during a seismic cycle (Figures 7g, h). When fluid is injected earlier (at year 7.94, 20% of the recurrence interval), both aseismic slip and seismic rupture occur earlier compared to the reference (at year 8.47, 50% of the recurrence interval). The seismic rupture occurs at year 8.77, representing a delay of ~0.83 years from the initiation of injection. Considering that the reference model exhibits a ~0.51-year offset between injection initiation and earthquake occurrence, we infer that earlier injection can lead to relatively delayed seismic events. The aseismic-slip events have a smaller V_{max} than the reference, but there are more events. Note that no additional aseismic event occurs after the injection is stopped. When fluid is injected at year 8.99 (80% of the recurrence interval), an aseismic slip event and an earthquake occur shortly after the injection (Figure 7h). The delay time between injection initiation and seismic rupture is ~0.2 years. We estimate the maximum stress state at the center of the fault prior to seismic ruptures, resulting in values of 35.11, 38.89, and 39.40 MPa for injections at 20%, 50%, and 80% of the recurrence intervals, respectively (Figure S10). This implies that the cumulative stress state on the fault plays a role in triggering seismic ruptures. Injection onset close to the end of the interseismic period triggers earthquakes 2.5 to 4 times more quickly compared to other simulations where fluid injection starts in the early or middle of the interseismic period. Based on these findings, we investigate the relationship between shear stress and pore-pressure perturbation across all simulated events from injection operation tests. For aseismic slip, shear stress states exhibit a positive correlation with pore-pressure values (slope = 5.10), whereas an inverse-proportional relationship is observed for seismic ruptures (slope = -0.63) (Figure S11). This opposite trend between aseismic and seismic events is consistent with the pattern observed between stress drop and pore-pressure perturbation (Figure 6d).

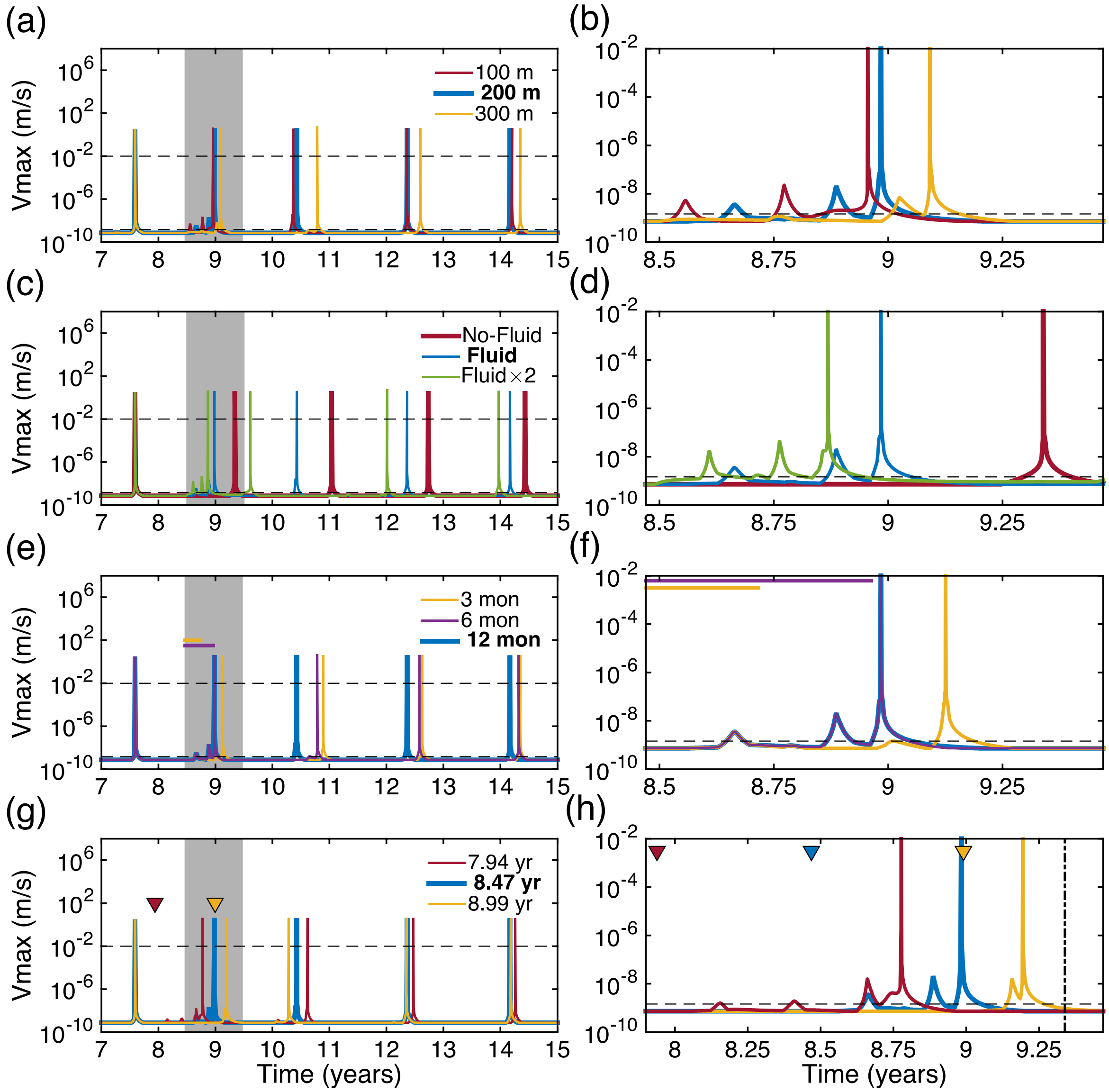

Figure 7. V_{max} over time for various injection scenarios. The left-hand column represents the long-term time period, while the right-hand column provides a zoomed-in view of the injection period. The different injection scenarios are as follows: (a, b) Injection at different locations: -100 m in red, -200 m in blue, and -300 m in orange; (c, d) Different injection volumes: twice the amount of injection volume (34.8 Pa/s) in green compared to the reference volume (17.4 Pa/s) in blue and zero volume in red; (e, f) Different injection durations: 3, 6, and 12 months displayed by orange, purple, and blue lines; (g, h) Different injection onset times: at years 7.94, 8.47, and 8.99, represented by red, blue, and orange. The colored horizontal lines in (e, f) indicate the duration of 3 and 6 months. Inverted triangles in (g, h) denote the onsets of fluid injection, and the vertical dashed line in (h) represents a coseismic rupture from a no-fluid simulation. In all figures, the horizontal dashed lines denote the threshold slip velocities that define seismic slip (10^{-2} m/s) and aseismic slip (1.46×10^{-9} m/s). The bold text in the legend corresponds to the reference model setup.

Figure 8 illustrates the source scaling of aseismic events derived from a number of injection settings shown in Figure 7. Stress-drop values from the early injection at year 7.94 and the 6-month injection duration show lower-stress drops (< 0.1 MPa) and moments (< 10^8 N·m), whereas the other aseismic-slip events mostly exhibit source parameters consistent with those estimated in the reference fluid-injection model (Figure 8a). In general, the occurrence of aseismic slip releases the stress accumulated during the interseismic period, potentially delaying seismic events (i.e., slip deficit). However, overpressure associated with fluid injection may prevent the accumulation of slip deficit associated with aseismic transients, ultimately advancing the occurrence of seismic rupture. In all simulations, the source scaling of aseismic-slip events is estimated to follow a relationship of $M_0 \propto r_0^{3.4}$ (Figure 8b). When including seismic ruptures in the scaling analysis, the relationship becomes $M_0 \propto r_0^{4.3}$, which is similar to the DFWA observations ($M_0 \propto r_0^{4.7}$). We acknowledge, however, that linear regression is estimated with a limited number of events with a small range of rupture radii and moments.

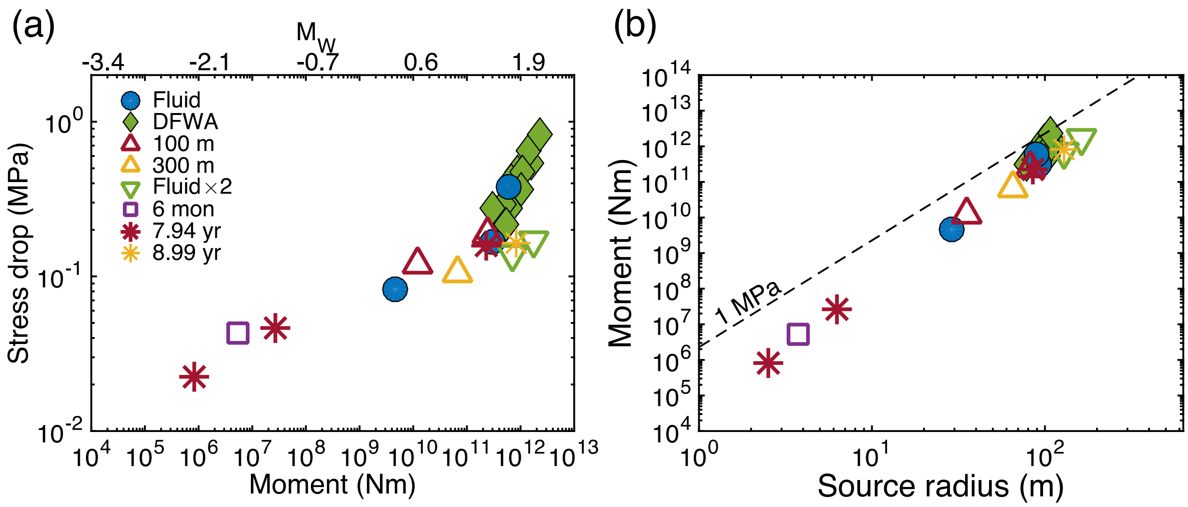

Figure 8. A comparison of source parameters resulting from various injection parameters shown in Figure 7. (a) displays stress drop as a function of the seismic moment. (b) illustrates moment against source radius. The simulations with varying separations between injection locations and the center of VW asperity (100 m in red and 300 m in orange) are represented by transparent triangles, while green inverted triangles and purple squares correspond to a twice larger injection volume and shorter injection duration (6 months). Asterisks indicate the scenarios with early injection at year 7.94 (red) and late injection at year 8.99 (orange). The observed values in the DFWA earthquake sequence (Jeong et al., 2022) are denoted by green diamonds. In (b), the dashed line represents a constant stress-drop relation of 1 MPa.

3.3.2 Effects of Fault Frictional Parameters

We conduct multiple simulations, varying fault frictional parameters (i.e., a, b, and d_c), to investigate the effects of fault friction on our model. First, we perform simulations with no-injection scenario. Since the purpose of this study is to investigate and quantify changes in seismic and aseismic slip patterns during and after injection, we do not consider simulations that do not generate seismic events within a simulation time of 15 years, as well as those that exhibit irregular recurrence intervals due to the presence of aseismic slip or partial rupture during the interseismic period (see details in Text S4 and Figures S12-S14 in Supporting information). After testing a wide range of frictional parameters, simulations that fit the above criteria have $(a-b)_{VW}$ ranging from -0.0050 to -0.0036, and d_c ranging from 40 to 220 μm. Based on these findings, we focus on fluid injection under three $(a-b)_{VW}$ scenarios: -0.0050, -0.0040, and -0.0036, each with different values of d_c. Simulations that exhibit smaller aseismic events below our threshold are subsequently excluded from the analysis. Recognizing that the injection at 20% of interseismic period leads to an increased number of aseismic-slip events from the injection operation tests (Figures 7g, h), we incorporate these earlier injection scenarios into the multiple fault parameter tests.

Figure 9 illustrates the source parameters estimated from slip produced under various fault frictional parameters in the fluid-injection model. Our simulations produce a wide spectrum of slip modes (events with a wide range of slip rates). The stress drops of seismic ruptures appear to be independent of the distance from the injector (Figure 9c). However, the stress-drop values are increased with increasing seismic moments (Figure 9a), and the scaling follows $M_0 \propto r_0^{3.46}$ (Figure 9b). In contrast, stress-drop values are decreased with increasing averaged pore-pressure perturbation with a slope of -0.92 (Figure 9d), which corresponds to the results from Figure 6d, suggesting that pore-pressure changes lead to a reduction in the stress-drop values of seismic ruptures. Consequently, the combination of fluid injection and various fault friction models produces a smooth pattern of stress drop as a function of moments (Figures 9a, b).

In the case of aseismic-slip events, the average stress drop value is 0.1 MPa, a factor of 10 lower than the average stress drop of seismic ruptures. Stress drop and moment values of aseismic-slip events exhibit a wide distribution, with some overlapping with the DFWA events (Figure 9a). The estimates for aseismic-stress drop show slight increases with distance from the injection point (slope = 0.42 on a log scale) and with pore-pressure perturbation (slope = 0.57 on a log scale) as shown in Figures 9c and 9d. The pore-pressure perturbations are higher than the stress-drop estimates by an average of ~0.13 MPa. The stress drop also increases with seismic moment, which is similar to those of seismic ruptures. The source scalings are $M_0 \propto r_0^{3.54}$, $M_0 \propto r_0^{3.53}$, and $M_0 \propto r_0^{3.63}$ for the least, reference, and most velocity-weakening faults, respectively. These source scaling relationships are consistent with the scaling estimated in various injection scenarios shown in section 3.3.1, $M_0 \propto r_0^{3.4}$, suggesting a similarity in the energy release patterns of the aseismic transients. When considering both seismic ruptures and aseismic-slip events, the scaling follows $M_0 \propto r_0^{4.4}$, closely resembling the scaling observed in the DFWA sequence, $M_0 \propto r_0^{4.7}$. Additionally, we investigate the effect of various thresholds for aseismic transients (Text S5 and Figures S15-17). Increasing the threshold leads to reduced moments and source radii, while stress drops increase, revealing more dynamic properties and connection between aseismic slip and seismic ruptures. Despite these alterations, the scaling relationships remain consistent with Figure 9b (Figure S16). Thus, the lower-stress-drop events within the DFWA sequence may represent less dynamic ruptures that sit in the transition of aseismic and seismic slip involved in a wide spectrum of slip modes as shown in our simulations. Detailed results from all simulations can be found in Datasets in the Supporting Information (Dataset S1 for aseismic events and Dataset S2 for seismic ruptures).

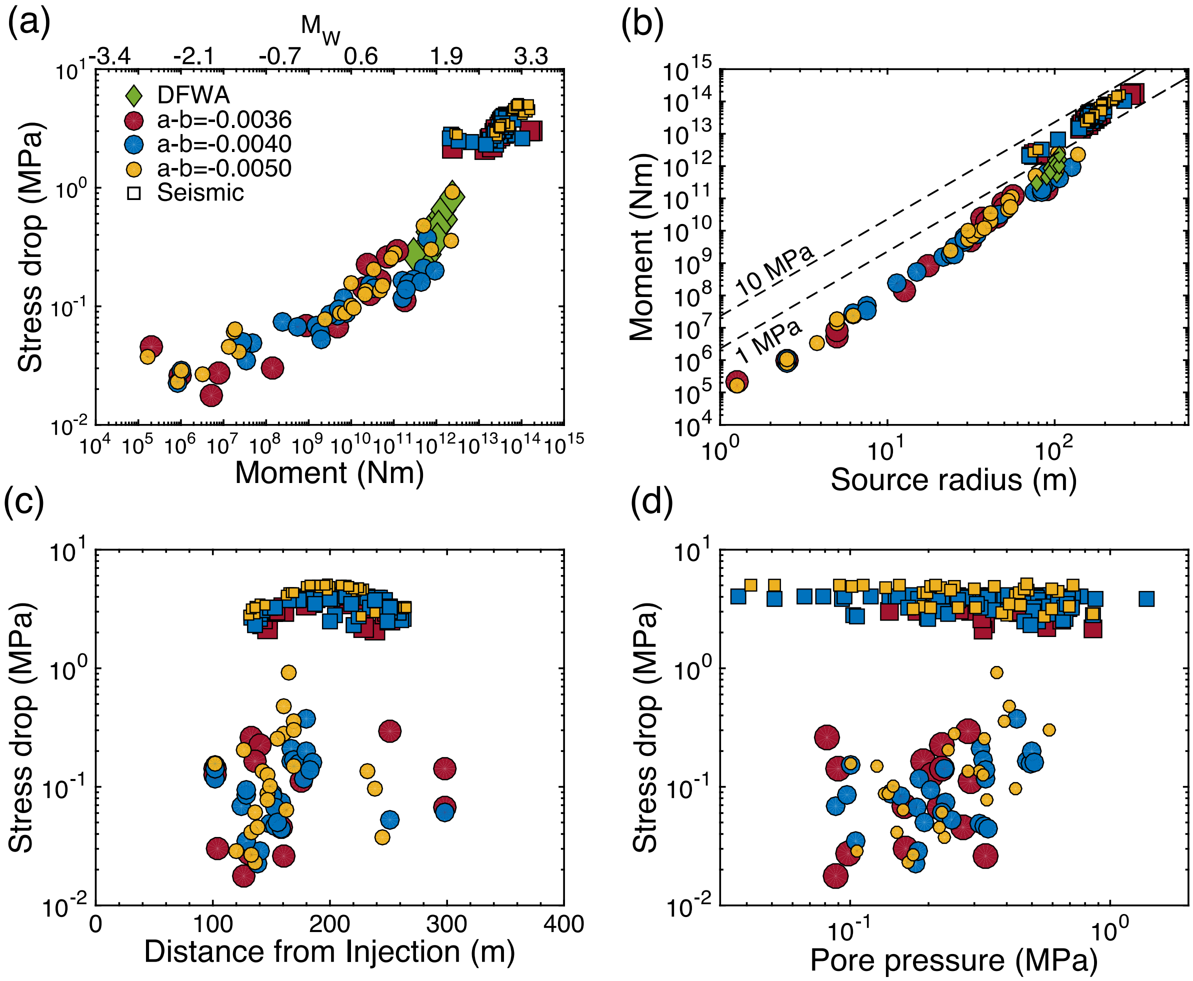

Figure 9. Source parameters obtained from different fault frictional parameters, with circles denoting aseismic slip and squares representing seismic ruptures. (a, c, d) display the relationships between stress drop and (a) seismic moment, (c) distance from the injection point, and (d) average pore-pressure change. (b) shows seismic moment as a function of source radius. The distinctions between three $(a-b)_{VW}$ scenarios: least (-0.0036), reference (-0.0040), and most velocity-weakening faults (-0.0050) are represented by various sizes and colors. In (a, b), the green diamonds depict observed stress drops in the DFWA sequence (Jeong et al., 2022). Dashed lines in (b) indicate constant stress drop values of 1 and 10 MPa.

4. Discussion

We conduct simulations of dynamic rupture on rate-and-state friction faults with spatially varying pore-pressure perturbations to investigate the source properties of injection-induced earthquakes. Our numerical modeling shows that injection-induced pore-pressure perturbations trigger a continuous spectrum of slip behavior ranging from aseismic slip to seismic rupture, consistent with previous studies (e.g., Guglielmi et al., 2015; Yu et al., 2021). Aseismic-slip events occur prior to the dynamic ruptures, which alter the timing and source parameters of subsequent seismic events. This supports the claims in earlier studies that injection-triggered aseismic slip contributes to the triggering of earthquakes (Bhattacharya & Viesca, 2019; Eyre et al., 2022). Simulations with various injection parameters and fault frictional parameters produce a wide spectrum of slip modes that share similar non-self-similar scaling, as observed in the DFWA sequence.

The key finding in our study is that fluid injection likely modifies the criticality of faults and hence the pattern of stress release, resulting in a broad spectrum of slip modes and their non-self-similar scaling. Changes in fluid pressure are widely recognized to cause transitions between stable and unstable slip behavior on faults (Bürgmann, 2018). The transition can occur when reduced shear strength or slip resistance leads to slip in a part of the asperity while the rest of the asperity remains strong. When faults are not fully locked during the interseismic period, stress perturbations associated with a fluid injection can cause the fault to release a portion of its energy (Ji et al., 2023). Numerical modeling by Marguin & Simpson (2023) suggest that fluid-pressure perturbations result in slow-slip events that have relatively lower stress drops, slip, and slip velocity. Another numerical modeling study by Lengliné et al. (2023) suggest that increased pore pressure may stabilize seismogenic patches and lead to a transition between seismic and aseismic behavior. Therefore, changes in effective normal stress may contribute to the non-self-similar source scaling observed in our modeling results.

Several studies have proposed heterogeneities on the fault as the cause of low-stress-drop events observed in induced seismicity. Yu et al. (2021) suggest that slow-slip events can occur due to fractured rock volume associated with fluid injection and hydraulic fracturing. These fractures can decrease pore pressure and increase effective normal stress, thereby inhibiting slip acceleration. Pennington et al. (2022) suggest that low-stress-drop events observed in injection-induced seismicity are derived from immature faults. For instance, the M_W 4.0 Guthrie earthquake occurred in a stronger VW area, while the low-stress-drop events of the first sequence occurred in a weaker slip patch. Through numerical simulations, Lin & Lapusta (2018) suggest that a complex fault shape with heterogeneous strength may produce stress-drop variations. In our study, a wide range of simulations with diverse frictional properties, which possibly capture the various extent of fault heterogeneity under the influence of fluid pressurization, produce a smooth and consistent scaling law comparable to those estimated by the DFWA sequence. These results support the notion that the observed low-stress-drop events may be related to the interplay between heterogeneity and the extent of pore-pressure perturbations along the faults as suggested by previous studies. However, our simplified single-VW-patch model does not consider interactions among asperities (e.g., Lui & Lapusta, 2016). Additionally, the linear combination of frictional heterogeneities in our model differs slightly from the heterogeneous fault suggested by previous studies, where the mechanical properties of the fault exhibit spatial variability. Thus, further research incorporating multiple asperities is necessary to comprehensively investigate the impacts of such heterogeneous faults.

Due to insufficient geological data for the properties of the DFWA fault, we establish a numerical framework with only one VW patch. The use of a simple model can offer a straightforward simulation and understanding (Lengliné et al., 2023), but such simplification also makes it challenging to produce a quantitative match to observations. The simple approach does not consider several factors, such as changes in dilatancy, thermal pressurization or flash weakening processes, and opening-mode fractures. These factors potentially provide additional mechanisms for reducing fluid pressure (Segall & Bradley, 2012; Yang & Dunham, 2021; Heimisson et al, 2022). Also, stress drops from numerical modeling are estimated following different procedures compared to those from observational calculations. We directly estimate the average shear stress changes from the simulation, whereas stress drops in observational studies are estimated from the averaged source spectrum recorded across multiple stations (Chen & Abercrombie, 2020; Huang et al., 2019; Jeong et al., 2022; Yu et al., 2021). The accuracy of these estimates depends on the number of stations, network coverage resolution, and rupture directivity (Kemna et al., 2020). In addition, stress-drop estimates can be biased by inappropriate path correction, especially depth-dependent attenuation factors (Abercrombie et al., 2021).

If the transition from aseismic to seismic behavior is a general phenomenon, then aseismic slip can be a precursor to the occurrence of seismic rupture. Danré et al. (2022) suggest that aseismic slip observed in induced seismicity has the same mechanism as the natural slow earthquakes that generally occur in a subduction zone. This finding suggests that we can potentially extend our findings from the study of induced earthquakes with known fluid input to understand the detailed fluid effect on natural earthquake slip at large. For instance, the fluid volume-seismicity relation estimated from induced earthquakes has been applied to represent the dynamic behavior of slab-derived fluid associated with natural earthquake swarms (Mukuhira et al., 2022). Hence, modeling of induced seismicity can improve our understanding of pore-pressure effects on earthquake swarms in natural conditions and can provide critical insights for the spatiotemporal evolution of seismicity and timing prediction as a precursor to large earthquakes (Ruhl et al., 2016). Additionally, changes in slip patterns or non-self-similar scaling during and after injection can be evidence that earthquakes were influenced by a fluid-driven source or human activities. Relatively slow earthquakes, different triggering mechanisms, and variations in seismicity patterns contribute to modifications in seismic hazard assessment (e.g., Petersen et al., 2016).

5. Conclusions

In this study, we investigate the interplay between fluid-pressure perturbations, aseismic slip, and seismic rupture in order to understand the source scaling of injection-induced earthquakes near the DFWA. Our findings show that changes in stress caused by injected fluid pressure can trigger aseismic-slip events that advance or delay subsequent seismic ruptures relative to models without fluid injection. Additionally, the susceptibility to trigger slip on a fault is likely dependent on the stage of its seismic cycle. Injecting fluid on a critically-stressed fault close to the next coseismic period induces earthquakes 2.5 to 4 times earlier than fluid injection in the middle of the interseismic period. The aseismic-slip events and fluid pressurization, together cause variation of source properties in subsequent seismic ruptures. Simulations involving various injection scenarios and fault frictional parameters suggest a positive correlation between pore-pressure perturbation and aseismic-stress drops (slope = 0.48). Conversely, for seismic events, the trend is reversed (slope = -0.92). This relationship results in a broad spectrum of slip modes, which shows a scaling between stress drop and moment following $M_0 \propto r_0^{4.4}$ for all simulated events. Based on the similar scaling observed in the DFWA sequence, $M_0 \propto r_0^{4.7}$, we suggest that lower-stress-drop events in the vicinity of the DFWA may signify less dynamic ruptures involved in a wide range of slip modes, as shown in our simulations.

Consequently, our model highlights the importance of monitoring aseismic signals close to injection operation, which may serve as precursors to more destructive fault ruptures.

Open Research

No data were used in this study. Simulation results are available in the tables provided by the online version of supporting information.

Acknowledgments

This study was supported by Roger E. Deane Post-Doctoral Fellowship through the Department of Earth Sciences at University of Toronto and the Natural Sciences and Engineering Research Council of Canada (Discovery Grants 2019-06482 to S.K.Y.L.). The numerical simulations were performed on the Niagara and Graham supercomputer at the SciNet HPC Consortium (Loken et al., 2010; Ponce et al., 2019). SciNet is funded by: The Canada Foundation of Innovation: the Government of Ontario; Ontario Research ORK-Research Excellence; and the University of Toronto.

References

Abercrombie, R. E., Trugman, D. T., Shearer, P. M., Chen, X., Zhang, J., Pennington, C. N., ... & Ruhl, C. J. (2021). Does earthquake stress drop increase with depth in the crust?. *Journal of Geophysical Research: Solid Earth*, *126*(10), e2021JB022314. https://doi.org/10.1029/2021JB022314

Ampuero, J. P., & Rubin, A. M. (2008). Earthquake nucleation on rate and state faults–Aging and slip laws. *Journal of Geophysical Research: Solid Earth*, *113*(B1). https://doi.org/10.1029/2007JB005082

Bhattacharya, P., & Viesca, R. C. (2019). Fluid-induced aseismic fault slip outpaces pore-fluid migration. *Science*, *364*(6439), 464-468. https://doi.org/10.1126/science.aaw7354

Blanpied, M. L., Lockner, D. A., & Byerlee, J. D. (1991). Fault stability inferred from granite sliding experiments at hydrothermal conditions. *Geophysical Research Letters*, *18*(4), 609-612. https://doi.org/10.1029/91GL00469

Blanpied, M. L., Lockner, D. A., & Byerlee, J. D. (1995). Frictional slip of granite at hydrothermal conditions. *Journal of Geophysical Research: Solid Earth*, *100*(B7), 13045-13064. https://doi.org/10.1029/95JB00862

Bürgmann, R. (2018). The geophysics, geology and mechanics of slow fault slip. *Earth and Planetary Science Letters*, *495*, 112-134. https://doi.org/10.1016/j.epsl.2018.04.062

Cappa, F., Scuderi, M. M., Collettini, C., Guglielmi, Y., & Avouac, J. P. (2019). Stabilization of fault slip by fluid injection in the laboratory and in situ. *Science advances*, *5*(3), eaau4065. https://doi.org/10.1126/sciadv.aau4065

Chen, X., & Abercrombie, R. E. (2020). Improved approach for stress drop estimation and its application to an induced earthquake sequence in Oklahoma. *Geophysical Journal International*, *223*(1), 233-253. https://doi.org/10.1093/gji/ggaa316

Chen, T., & Lapusta, N. (2009). Scaling of small repeating earthquakes explained by interaction of seismic and aseismic slip in a rate and state fault model. *Journal of Geophysical Research: Solid Earth*, *114*(B1). https://doi.org/10.1029/2008JB005749

Danré, P., De Barros, L., Cappa, F., & Ampuero, J. P. (2022). Prevalence of aseismic slip linking fluid injection to natural and anthropogenic seismic swarms. *Journal of Geophysical Research: Solid Earth*, *127*(12), e2022JB025571. https://doi.org/10.1029/2022JB025571

De Barros, L., Guglielmi, Y., Cappa, F., Nussbaum, C., & Birkholzer, J. (2023). Induced microseismicity and tremor signatures illuminate different slip behaviours in a natural shale fault reactivated by a fluid pressure stimulation (Mont Terri). *Geophysical Journal International*, *235*(1), 531-541. https://doi.org/10.1093/gji/ggad231

DeShon, H. R., Hayward, C. T., Ogwari, P. O., Quinones, L., Sufri, O., Stump, B., & Magnani, M. B. (2019). Summary of the North Texas earthquake study seismic networks, 2013–2018. *Seismological Research Letters*, *90*(1), 387-394. https://doi.org/10.1785/0220180269

Dieterich, J. H. (1979). Modeling of rock friction: 1. Experimental results and constitutive equations. *Journal of Geophysical Research*, *84*(B5), 2161–2168. https://doi.org/10.1029/jb084ib05p02161

Durand, V., Gualandi, A., Ergintav, S., Kwiatek, G., Haghshenas, M., Motagh, M., Dresen, G., Martinez Garzon, P. (2022). Deciphering aseismic deformation along submarine fault branches below the eastern Sea of Marmara (Turkey): Insights from seismicity, strainmeter, and GNSS data. *Earth and Planetary Science Letters*, *594*, 117702. https://doi.org/10.1016/j.epsl.2022.117702

Ellsworth, W. L. (2013). Injection-induced earthquakes. *science*, *341*(6142), 1225942. https://doi.org/10.1126/science.1225942

Eshelby, J. D. (1957). The determination of the elastic field of an ellipsoidal inclusion, and related problems. *Proceedings of the royal society of London. Series A. Mathematical and physical sciences*, *241*(1226), 376-396. http://www.jstor.org/stable/100095

Eyre, T. S., Samsonov, S., Feng, W., Kao, H., & Eaton, D. W. (2022). InSAR data reveal that the largest hydraulic fracturing-induced earthquake in Canada, to date, is a slow-slip event. *Scientific reports*, *12*(1), 2043. https://doi.org/10.1038/s41598-022-06129-3

Foulger, G. R., Wilson, M. P., Gluyas, J. G., Julian, B. R., & Davies, R. J. (2018). Global review of human-induced earthquakes. *Earth-Science Reviews*, *178*, 438-514. https://doi.org/10.1016/j.earscirev.2017.07.008

Frohlich, C., Hayward, C., Stump, B., & Potter, E. (2011). The Dallas–Fort Worth earthquake sequence: October 2008 through May 2009. *Bulletin of the Seismological Society of America*, *101*(1), 327-340. https://doi.org/10.1785/0120100131

Gao, S., Nicot, J. P., Hennings, P. H., La Pointe, P., Smye, K. M., Horne, E. A., & Dommisse, R. (2021). Low pressure buildup with large disposal volumes of oil field water: A flow model of the Ellenburger Group, Fort Worth Basin, northcentral Texas. *AAPG Bulletin*, *105*(12), 2575-2593. https://doi.org/10.1306/03252120159

Goertz-Allmann, B. P., Goertz, A., & Wiemer, S. (2011). Stress drop variations of induced earthquakes at the Basel geothermal site. *Geophysical Research Letters*, *38*, L09308. https://doi.org/10.1029/2011GL047498

Guglielmi, Y., Cappa, F., Avouac, J. P., Henry, P., & Elsworth, D. (2015). Seismicity triggered by fluid injection–induced aseismic slip. *Science*, *348*(6240), 1224-1226. https://doi.org/10.1126/science.aab0476

Häring, M. O., Schanz, U., Ladner, F., & Dyer, B. C. (2008). Characterisation of the Basel 1 enhanced geothermal system. *Geothermics*, 37(5), 469-495. https://doi.org/10.1016/j.geothermics.2008.06.002

Harris, R. A. (2017). Large earthquakes and creeping faults. *Reviews of Geophysics*, *55*(1), 169-198. https://doi.org/10.1002/2016RG000539

Heimisson, E. R., Liu, S., Lapusta, N., & Rudnicki, J. (2022). A Spectral Boundary-Integral Method for Faults and Fractures in a Poroelastic Solid: Simulations of a Rate-and-State Fault With Dilatancy, Compaction, and Fluid Injection. *Journal of Geophysical Research: Solid Earth*, *127*(9), e2022JB024185. https://doi.org/10.1029/2022JB024185

Hennings, P. H., Snee, J. E. L., Osmond, J. L., DeShon, H. R., Dommisse, R., Horne, E., ... & Zoback, M. D. (2019). Injection-induced seismicity and fault-slip potential in the Fort Worth Basin, Texas. *Bulletin of the Seismological Society of America*, *109*(5), 1615-1634. https://doi.org/10.1785/0120190017

Hornbach, M. J., DeShon, H. R., Ellsworth, W. L., Stump, B. W., Hayward, C., Frohlich, C., ... & Luetgert, J. H. (2015). Causal factors for seismicity near Azle, Texas. *Nature communications*, *6*(1), 6728. https://doi.org/10.1038/ncomms7728

Horne, E. A., Hennings, P. H., Osmond, J. L., & DeShon, H. R. (2020). Structural characterization of potentially seismogenic faults in the Fort Worth Basin. *Interpretation*, *8*(2), T323-T347. https://doi.org/10.1190/INT-2019-0188.1

Huang, Y., De Barros, L., & Cappa, F. (2019). Illuminating the rupturing of microseismic sources in an injection-induced earthquake experiment. *Geophysical Research Letters*, *46*(16), 9563–9572. https://doi.org/10.1029/2019gl083856

Jeong, S. J., Stump, B. W., & DeShon, H. R. (2022). Stress drop variations of induced earthquakes near the Dallas–Fort Worth Airport, Texas. *The Seismic Record*, *2*(2), 68-77. https://doi.org/10.1785/0320220003

Ji, Y., Zhang, W., Hofmann, H., Chen, Y., Kluge, C., Zang, A., & Zimmermann, G. (2023). Modelling of fluid pressure migration in a pressure sensitive fault zone subject to cyclic injection and implications for injection-induced seismicity. *Geophysical Journal International*, *232*(3), 1655-1667. https://doi.org/10.1093/gji/ggac416

Jiang, Y., Samsonov, S. V., & González, P. J. (2022). Aseismic fault slip during a shallow normal-faulting seismic swarm constrained using a physically informed geodetic inversion method. *Journal of Geophysical Research: Solid Earth*, *127*(7), e2021JB022621. https://doi.org/10.1029/2021JB022621

Kemna, K. B., Peña Castro, A. F., Harrington, R. M., & Cochran, E. S. (2020). Using a large-n seismic array to explore the robustness of spectral estimations. *Geophysical Research Letters*, *47*(21), e2020GL089342. https://doi.org/10.1029/2020GL089342

Khajehdehi, O., Karimi, K., & Davidsen, J. (2022). The effect of correlated permeability on fluid-induced seismicity. *Geophysical Research Letters*, *49*(4), e2021GL095199. https://doi.org/10.1029/2021GL095199

Kreemer, C., Hammond, W. C., & Blewitt, G. (2018). A robust estimation of the 3-D intraplate deformation of the North American plate from GPS. *Journal of Geophysical Research: Solid Earth*, *123*(5), 4388-4412. https://doi.org/10.1029/2017JB015257

Lapusta, N., & Liu, Y. (2009). Three-dimensional boundary integral modeling of spontaneous earthquake sequences and aseismic slip. *Journal of Geophysical Research: Solid Earth*, *114*(B9), B09303. https://doi.org/10.1029/2008jb005934

Lapusta, N., Rice, J. R., Ben-Zion, Y., & Zheng, G. (2000). Elastodynamic analysis for slow tectonic loading with spontaneous rupture episodes on faults with rate- and state-dependent friction. *Journal of Geophysical Research*, *105*(B10), 23765–23789. https://doi.org/10.1029/2000jb900250

Larochelle, S., Lapusta, N., Ampuero, J. P., & Cappa, F. (2021). Constraining fault friction and stability with fluid-injection field experiments. *Geophysical Research Letters*, *48*(10), e2020GL091188. https://doi.org/10.1029/2020GL091188

Lee, K. K., Ellsworth, W. L., Giardini, D., Townend, J., Ge, S., Shimamoto, T., ... & Langenbruch, C. (2019). Managing injection-induced seismic risks. *Science*, *364*(6442), 730-732. https://doi.org/10.1126/science.aax1878

Lengliné, O., Ampuero, J. P., & Schmittbuhl, J. (2023). Scaling of repeating earthquakes at the transition from aseismic to seismic slip. *Geophysical Research Letters*, *50*(12), e2022GL101604. https://doi.org/10.1029/2022GL101604

Lin, Y. Y., & Lapusta, N. (2018). Microseismicity simulated on asperity-like fault patches: On scaling of seismic moment with duration and seismological estimates of stress drops. *Geophysical Research Letters*, *45*(16), 8145-8155. https://doi.org/10.1029/2018GL078650

Loken, C., Gruner, D., Groer, L., Peltier, R., Bunn, N., Craig, M., et al. (2010). SciNet: Lessons learned from building a power-efficient top-20 system and data center. *Journal of Physics*, *256*, 012026. https://doi.org/10.1088/1742-6596/256/1/012026

Lui, S. K., Huang, Y., & Young, R. P. (2021). The role of fluid pressure-induced aseismic slip in earthquake cycle modulation. *Journal of Geophysical Research: Solid Earth*, *126*(4), e2020JB021196. https://doi.org/10.1029/2020JB021196

Lui, S. K., & Lapusta, N. (2016). Repeating microearthquake sequences interact predominantly through postseismic slip. *Nature communications*, *7*(1), 13020. https://doi.org/10.1038/ncomms13020

Marone, C. (1998). Laboratory-derived friction laws and their application to seismic faulting. *Annual Review of Earth and Planetary Sciences*, *26*(1), 643–696. https://doi.org/10.1146/annurev.earth.26.1.643

Magnani, M. B., Blanpied, M. L., DeShon, H. R., & Hornbach, M. J. (2017). Discriminating between natural versus induced seismicity from long-term deformation history of intraplate faults. *Science advances*, *3*(11), e1701593. https://doi.org/10.1126/sciadv.1701593

Marguin, V., & Simpson, G. (2023). Influence of fluids on earthquakes based on numerical modeling. *Journal of Geophysical Research: Solid Earth*, *128*(2), e2022JB025132. https://doi.org/10.1029/2022JB025132

Moreno, M., Rosenau, M., & Oncken, O. (2010). 2010 Maule earthquake slip correlates with pre-seismic locking of Andean subduction zone. *Nature*, *467*(7312), 198-202. https://doi.org/10.1038/nature09349

Mukuhira, Y., Uno, M., & Yoshida, K. (2022). Slab-derived fluid storage in the crust elucidated by earthquake swarm. *Communications Earth & Environment*, *3*(1), 286. https://doi.org/10.1038/s43247-022-00610-7

National Research Council (2013). *Induced seismicity potential in energy technologies*. 255 pp., National Academies Press, Washington, D.C., https://doi.org/10.17226/13355

Noda, H., Lapusta, N., & Kanamori, H. (2013). Comparison of average stress drop measures for ruptures with heterogeneous stress change and implications for earthquake physics. *Geophysical Journal International*, *193*(3), 1691–1712. https://doi.org/10.1093/gji/ggt074

Obara, K., & Kato, A. (2016). Connecting slow earthquakes to huge earthquakes. *Science*, *353*, 253-257. https://doi.org/10.1126/science.aaf1512

Ogwari, P. O., DeShon, H. R., & Hornbach, M. J. (2018). The Dallas-Fort Worth airport earthquake sequence: Seismicity beyond injection period. *Journal of Geophysical Research: Solid Earth*, *123*(1), 553-563. https://doi.org/10.1002/2017JB015003

Pennington, C. N., Uchide, T., & Chen, X. (2022). Slip characteristics of induced earthquakes: insights from the 2015 Mw 4.0 Guthrie, Oklahoma earthquake. *Journal of Geophysical Research: Solid Earth*, *127*(5), e2021JB023564. https://doi.org/10.1029/2021JB023564

Pepin, K. S., Ellsworth, W. L., Sheng, Y., & Zebker, H. A. (2022). Shallow aseismic slip in the Delaware basin determined by Sentinel-1 InSAR. *Journal of Geophysical Research: Solid Earth*, *127*(2), e2021JB023157. https://doi.org/10.1029/2021JB023157

Perry, S. M., Lambert, V., & Lapusta, N. (2020). Nearly magnitude-invariant stress drops in simulated crack-like earthquake sequences on rate-and-state faults with thermal pressurization of pore fluids. *Journal of Geophysical Research: Solid Earth*, *125*(3), e2019JB018597. https://doi.org/10.1029/2019JB018597

Petersen, M. D., Mueller, C. S., Moschetti, M. P., Hoover, S. M., Llenos, A. L., Ellsworth, W. L., ... & Rukstales, K. S. (2016). Seismic-hazard forecast for 2016 including induced and natural earthquakes in the central and eastern United States. *Seismological Research Letters*, *87*(6), 1327-1341. https://doi.org/10.1785/0220160072

Ponce, M., van Zon, R., Northrup, S., Gruner, D., Chen, J., Ertinaz, F., et al. (2019). Deploying a top-100 supercomputer for large parallel workloads: The Niagara supercomputer. In *Proceedings of the practice and experience in advanced Research computing on rise of* *the machines (learning)* (pp. 1–8). New York, NY, USA: Association for Computing Machinery. Retrieved from https://doi.org/10.1145/3332186.3332195

Quinones, L., DeShon, H. R., Jeong, S., Ogwari, P., Sufri, O., Holt, M. M., & Kwong, K. B. (2019). Tracking induced seismicity in the Fort Worth Basin: A summary of the 2008–2018 North Texas earthquake study catalog. *Bulletin of the Seismological Society of America*, *109*(4), 1203-1216. https://doi.org/10.1785/0120190057

Quinones, L. A., DeShon, H. R., Magnani, M. B., & Frohlich, C. (2018). Stress orientations in the Fort Worth Basin, Texas, determined from earthquake focal mechanismsstress orientations in the fort worth basin. *Bulletin of the Seismological Society of America*, *108*(3A), 1124-1132. https://doi.org/10.1785/0120170337

Rubin, A. M., & Ampuero, J.-P. (2005). Earthquake nucleation on (aging) rate and state faults. *Journal of Geophysical Research: Solid Earth*, *110*(B11). https://doi.org/10.1029/2005JB003686

Ruhl, C. J., Abercrombie, R. E., Smith, K. D., & Zaliapin, I. (2016). Complex spatiotemporal evolution of the 2008 Mw 4.9 Mogul earthquake swarm (Reno, Nevada): Interplay of fluid and faulting. *Journal of Geophysical Research: Solid Earth*, *121*(11), 8196–8216. https://doi.org/10.1002/2016jb013399

Ruina, A. (1983). Slip instability and state variable friction laws. *Journal of Geophysical Research*, *88*(B12), 10359–10370. https://doi.org/10.1029/jb088ib12p10359

Schaal, N., & Lapusta, N. (2019). Microseismicity on patches of higher compression during larger-scale earthquake nucleation in a rate-and-state fault model. *Journal of Geophysical Research: Solid Earth*, *124*(2), 1962–1990. https://doi.org/10.1029/2018jb016395

Segall, P., & Bradley, A. M. (2012). Slow-slip evolves into megathrust earthquakes in 2D numerical simulations. *Geophysical Research Letters*, *39*(18). https://doi.org/10.1029/2012GL052811

Shen, L., Zhao, L. F., Xie, X. B., He, X., Wang, W. M., & Yao, Z. X. (2023). Stress drop variations of the 2019 M_L 6.0 Changning earthquake and its aftershock sequence in the southern Sichuan Basin, China. *Tectonophysics*, 230139. https://doi.org/10.1016/j.tecto.2023.230139

Smye, K. M., Lemons, C. R., Eastwood, R., McDaid, G., & Hennings, P. H. (2019). Stratigraphic architecture and petrophysical characterization of formations for deep disposal in the Fort Worth Basin, Texas. *Interpretation*, *7*(4), SL1-SL17. https://doi.org/10.1190/int-2018-0195.1

Staniewicz, S., Chen, J., Lee, H., Olson, J., Savvaidis, A., Reedy, R., et al. (2020). InSAR reveals complex surface deformation patterns over an 80,000 km^2 oil-producing region in the Permian Basin. *Geophysical Research Letters*, *47*(21), e2020GL090151. https://doi.org/10.1029/2020GL090151

Wang, G., Greuter, A., Petersen, C. M., & Turco, M. J. (2022). Houston GNSS network for subsidence and faulting monitoring: Data analysis methods and products. *Journal of Surveying Engineering*, *148*(4), 04022008. https://doi.org/10.1061/(ASCE)SU.1943-5428.00003

Yang, Y., & Dunham, E. M. (2021). Effect of porosity and permeability evolution on injection-induced aseismic slip. *Journal of Geophysical Research: Solid Earth*, *126*(7), e2020JB021258. https://doi.org/10.1029/2020JB021258

Yu, H., Harrington, R. M., Kao, H., Liu, Y., & Wang, B. (2021). Fluid-injection-induced earthquakes characterized by hybrid-frequency waveforms manifest the transition from aseismic to seismic slip. *Nature communications*, *12*(1), 6862. https://doi.org/10.1038/s41467-021-26961-x

Zhai, G., & Shirzaei, M. (2018). Fluid injection and time-dependent seismic hazard in the Barnett Shale, Texas. *Geophysical Research Letters*, *45*(10), 4743-4753. https://doi.org/10.1029/2018GL077696

References From the Supporting Information

Cattania, C., & Segall, P. (2019). Crack models of repeating earthquakes predict observed moment-recurrence scaling. *Journal of Geophysical Research: Solid Earth*, *124*(1), 476-503. https://doi.org/10.1029/2018JB016056

Yin, Y., Galvez, P., Heimisson, E. R., & Wiemer, S. (2023). The role of three-dimensional fault interactions in creating complex seismic sequences. *Earth and Planetary Science Letters*, *606*, 118056. https://doi.org/10.1016/j.epsl.2023.118056

Zhu, W., Allison, K. L., Dunham, E. M., & Yang, Y. (2020). Fault valving and pore pressure evolution in simulations of earthquake sequences and aseismic slip. *Nature communications*, *11*(1), 4833. https://doi.org/10.1038/s41467-020-18598-z